Report on the closing theme
"Multimodal platform for Raman and nonlinear optical microscopy and microspectroscopy for condensed matter studies".

Theme code: 04-4-1111-2013/2017
Laboratory: Frank Laboratory of Neutron Physics
Department: Sector of Raman spectroscopy
Theme leader: G.M. Arzumanyan
Project leader: N. Kučerka

CONTENT

1. Introduction to Raman and CARS microscopy
2. The upgraded in 2015 laser scanning "CARS" microscope
3. Research programme
4. Student programme and international cooperation
5. Main publications and patent

Activities in 2015-2017 were implemented in accordance with the research programme and the main tasks listed within the theme "A multimodal platform for Raman and nonlinear optical microscopy and microspectroscopy for condensed matter studies" in the JINR Topical Plan.

The main functionality of the optical platform is based on the spectroscopy and microscopy of spontaneous Raman scattering and its nonlinear modification – stimulated coherent Raman scattering, known as CARS – Coherent Anti-Stokes Raman Scattering.

1. Introduction to Raman and CARS microscopy

Raman spectroscopy has been recognized to be a powerful tool for bioanalytical and biomedical applications because Raman spectra probe molecular vibrations that provide a highly specific fingerprint of the molecular structure and biochemical composition of tissues without external markers. In principle, diseases and other pathological anomalies lead to chemical and structural changes on the molecular level which also change the vibrational spectra and which can be used as sensitive, phenotypic markers of the disease. As these spectral changes are very specific and unique, they are also called fingerprint. The advantages of the methods include that they are non-destructive and do not require extrinsic contrast-enhancing agents.

Confocal and multiphoton imaging techniques are still the promising methods to perform sophisticated studies on biological samples. CARS microscopy provides an advanced, minimally invasive (nondestructive) and label-free technique with high sensitivity and high lateral spatial resolution capable of selective chemical imaging of major types of macromolecules: proteins, lipids,

nucleic acids, etc. Like spontaneous Raman, CARS probes vibrational modes in molecules and does not require exogenous dyes or markers, which is advantageous in imaging small molecules for which labeling may strongly affect their molecular properties.

CARS is a third-order, nonlinear optical process involving interactions between a pump beam of frequency ω_p, a Stokes beam of frequency ω_s, and a CARS signal at the anti-Stokes frequency of $\omega_{as}=2\omega_p-\omega_s$ (**Fig.1a**) generated in the phase matching direction (**Fig.1c**) . The vibrational contrast in CARS is created when the frequency difference $\Delta\omega=\omega_p-\omega_s$ between the pump and the Stokes beams is tuned to be resonant with a given vibration mode of a selected chemical bond. In this case the resonant oscillators are coherently driven by the excitation fields, thereby generating a strong and directed anti-Stokes signal compared to a spontaneous Raman scattering signal, for which Stokes and anti-Stokes photons are emitted incoherently. CARS signals are 3-4 orders of magnitude stronger than those of the spontaneous Raman process.

The anti-Stokes CARS signal frequency is blue-shifted from the both excitation frequencies and is easily detected in a spectral range free from the linear one-photon fluorescence background. However, the sensitivity of the forward CARS (F-CARS) signal was limited by the nonresonant background from any analyte and surrounding solvents (**Fig.1b**).
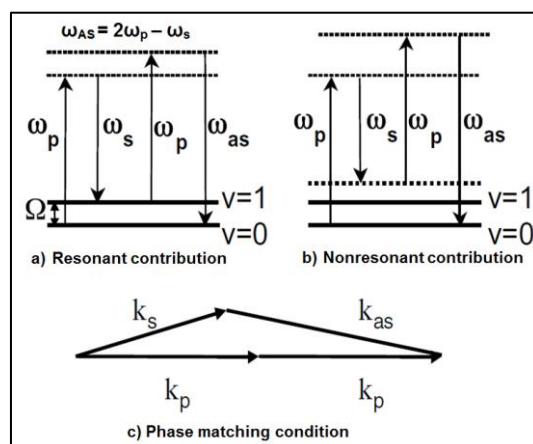

Fig.1. Energy diagram of CARS process

The nonresonant background arises from electronic contributions to the third order susceptibility $\chi(3)$ with no vibrational contrast and need to be minimized. There are several methods developed to improve the signal background ration including polarization sensitive detection, time-resolved detection and phase control of excitation pulses. As the CARS microscopy is a coherent imaging process it assumes strongly-defined phase relation of the induced polarization to the excitation fields. Thus, the resonant signal can be separated from the nonresonant background when polarization sensitive detection of CARS signal is employed (P-CARS) resulting in the enhanced image quality and contrast.

One of the main advantages of nonlinear optical microscopy is a high spatial resolution. In our CARS microscopy it is achieved with two collinearly overlapped near infrared picosecond beams and a water-immersion objective with a high numerical aperture. Furthermore, since the CARS intensity has a quadratic dependence on the pump field intensity and a linear dependence on the Stokes field intensity, the signal is generated only from a small volume in the central focal

region, providing CARS microscopy with a high 3D sectioning capability without the need of confocal geometry.

In comparison with conventional Raman imaging, CARS speeds up data acquisition from hours to seconds. Hence, with CARS we can provide a method of fast imaging (one image of 512x512 pixels can be obtained in a few seconds) demonstrating the structure of a bio-sample without any staining. All these above mentioned advantages demonstrated the unique possibilities of CARS microscopy over spontaneous Raman microscopy: high sensitivity, high speed and low photo damage.

2. The upgraded in 2015 laser scanning "CARS" microscope

Basic parameters:

As with any laser scanning microscope, the "CARS" platform recorded medium response to the influence of the laser radiation. Laser radiation can excite luminescence (single-photon and multi-photon), spontaneous and stimulated Raman scattering (CARS), other nonlinear effects (e.g. harmonic generation, sum and differential frequency), Rayleigh scattering, etc. For Raman signals a He-Ne laser (Melles Griot model 05-LHP-991) is installed with an output power of 10 mW at the wavelength of 632.8 nm and a beam divergence of less than 1 mrad. The laser beam was focused into the sample by means of a 40x or 100x microobjective lenses with a numerical aperture of 0.6 and 0.95 respectively. Microobjective lens is mounted on the piezo-stage providing Z-scanning in the range of 80 microns with a minimum step of 200 nm. The spectrum is analyzed with the monochromator-spectrograph MS-5004i, CCD camera and PMT.

It's well-known that the pulse duration of several picoseconds is a proper compromise between high intensity and narrow spectral bandwidth necessary for the CARS microscopy [15]. Besides, its intensity is sufficient also for detection of other nonlinear processes, in particular second and sum harmonic generation. Thus, a picosecond Nd:YVO4 tunable laser (EKSPLA, PT257-SOPO, Lithuania) with a pulse width of ~6ps, average power − 5W, and a repetition rate of 85 MHz is used as the source of the Stokes wave (ω_s) and is simultaneously used to synchronously pump an intracavity-doubled crystal optical parametric oscillator (SOPO). Thereby, the SOPO coherent device provides temporal synchronization with the Nd:YVO$_4$ and serves as a source of the pump beam (ω_p) tunable from 690nm to 990nm with a maximum output power of 200mW with a nearly Fourier transform-limited linewidth (~6cm-1). Only a small portion of biologically tolerable laser power is used for CARS and SONICC imaging.

We exploit parallel orientations of linear polarizations of the input Stokes and pump beams. Both excitation picosecond pulse trains are made coincident in time and in space utilizing an optical delay line and a series of dichroic mirrors. For CARS microscopy, we use a water-immersion objective lens with a high numerical aperture (NA=1.2, UPLANAPO-60x, Olympus) to focus the beams tightly. With the tight foci, the phase-matching conditions are relaxed because of the large cone of wave vectors of the excitation beams and the short interaction length.

Using our optical platform, a sample can be imaged by utilizing vibration frequencies in the spectral range of (1000−3580) cm−1, which covers all most important vibrational modes of bio-

molecules. Five detection channels allow two forward- and three backward- propagated signals to be recorded.

Four registration channels are installed at the platform for simultaneous high-speed measurements:
- F-CARS (Forward CARS)
- E-CARS & Raman (EPI direction)
- reflected signal
- transmitted signal

Upgraded in 2015 modalities:

For the implementation of the theme research programme for 2015-2017 and to be in line with the modern developments in this area, in 2015 the activities of the Sector of Raman Spectroscopy at FLNP were focused on the upgrade programme and further enlargement of the spectral and microscopic capabilities and features of the optical platform with the aim to implement the following new options:
- *Polarization sensitive Coherent antiStokes Raman Scattering (P-CARS)*
- *Second Order Nonlinear Imaging of Chiral Crystals (SONICC)*
- *Surface Enhanced Raman Scattering (SERS)*
- *Raman scattering using laser at 785 nm wavelength*
- *Raman scattering using laser at 532 nm wavelength*

All the above mentioned options were successfully elaborated and established at the "CARS" microscope. Fig.2 shows the upgraded schematic of the multimodal optical platform for performing Raman, P-CARS, SONICC (SHG), SERS spectroscopy and microscopy.
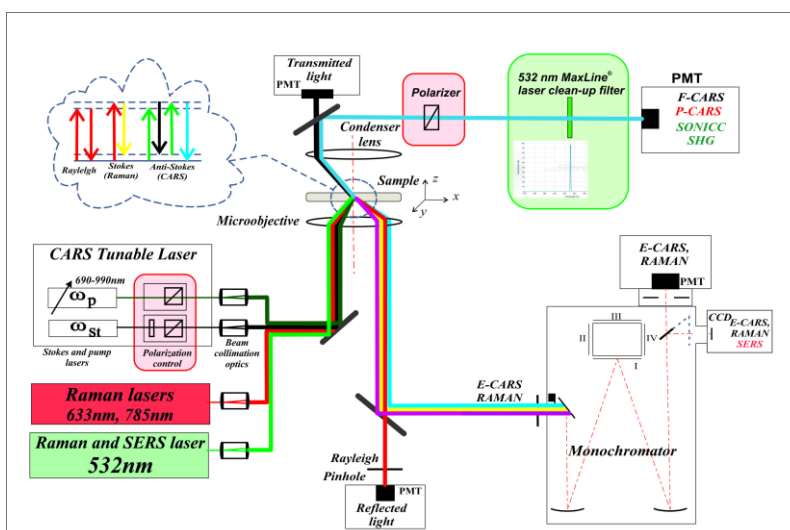

Fig.2. Diagram of the upgraded multimodal optical platform: "CARS" microscope

At present, using our optical platform, a sample can be imaged by utilizing vibration frequencies in the spectral range of (1000−3580) cm−1, which covers all most important vibrational modes of biomolecules.

The major drawback of CARS is the existence of a non-resonant background that arises from the electronic contributions even in the absence of vibrational resonance. In forward detected CARS (F-CARS) microscopy, the image contrast is limited by the background from the solvent (e.g., water). By taking advantage of the Raman depolarization ratio of certain modes, the resonant signal can be separated from the nonresonant background when polarization sensitive detection is employed In our scheme we employed Glan-Taylor polarizer installed on a rotation mount directed to the photomultiplier (Hamamatsu, H6780-01). The polarization control is adjustable with a half-wave plate in the Stokes beam (**Fig.2**). **P-CARS mapping significantly enhances the image quality by eliminating the nonresonant background almost completely.**

SONICC relies on second harmonic generation (SHG) scattering, which eliminates virtually all background from randomly oriented molecules, but generates a strong signal from chiral molecules arranged in a crystal [11-13]. Chiral crystals are those that lack an internal plane of symmetry, so only crystals that lack inversion symmetry will produce a signal. Most salt crystals are symmetrical and therefore generate no SHG, whereas all protein crystals are chiral and will generate a SHG signal. SONICC, however, does not distinguish between crystals of proteins and other chiral molecules, including some salts and small molecules that may be present in an analyte bio-sample. This may result in false positives when imaged in SONICC.

As for the SONICC imaging we exploit the same PMT for detection of P-CARS signals (see Fig.2). The Stokes wave served for second harmonic generation (532nm) in our samples, and a narrow bandpass filter (Semrock, FF01-532/3-25) was installed for a SHG signal filtration and further detection on the PMT.

Additionally to the above mentioned options, in 2015 we also incorporate into the our optical system and collinearly aligned with other lasers a diode-pumped cw single longitudinal mode green laser at 532nm with an adjustable output power of up to 20 mW and more than 50 meters coherence length (model SLM-417-20). This laser we used mainly for our SERS experiments with suitable for this wavelength SERS-active substrates covered with silver nanoparticles.

Along with the CARS and SONICC signals, the system allows detection of spontaneous Raman signals using three different lasers at 633nm and 785nm, luminescence (including up-conversion luminescence), second and sum frequency generation signals, reflection and transmission modes as well.

A computer-controlled XY galvanometer scanner (GSI-Lumonics VM1000) provided a fast scan of the sample in the lateral focal plane of the objective. All the CARS and SONICC images presented in this paper are composed of 500x500 pixels (250,000 pixels) taken by raster scanning the sample at room temperature. The corresponding bars are mentioned in the figures as well. Signal integration time was 3 µs/pixel resulting in a total acquisition time of 3s (including an image transfer time and an image visualization time). The objective lens is mounted on a computer-controlled z-axis translation piezostage for scanning through the microscope's optical axis with a minimal scan step of 0.1µm.

Table 1. Upgraded parameters of the "CARS" microscope

Main operating options	Raman, F-CARS, E-CARS, P-CARS, SERS, SECARS, luminescence, including upconversion
Lasers for Raman	532nm (15mW), 633nm (10mW), 785nm (100mW)
Laser for CARS	<u>Picosecond Nd:YVO4 laser: Ekspla, PT257 + SOPO</u> Stokes wavelength: 1064nm with pulse duration 6ps, 5W Tunable pump wavelength: 690-990nm, 5ps, 150-300 mW Pulse repetition rate: 85 MHz Mode composition: TEM_{00} Polarization: horizontal
Detection options	Five channels for high-speed measurements: Raman, CARS, reflected, transmitted, luminescent
Spectral detectable range	CARS signals: $990 - 5000$ cm^{-1} Raman signals: $75 - 6000$ cm^{-1}
Spectral resolution	CARS signals: 7-8 cm^{-1} Raman signals: 1.8 cm^{-1} (grating 600 g/mm)
Spatial resolution	CARS signals: < 0.7 µm Raman signals: XY: < 300 nm, Z: ~ 700 nm
Scanning range (fast mode, 60x lens)	XY: 225 x 225 µm Z: 80 µm
Spectral measurements and imaging	Monochromator/spectrograph MS5004i Digital CCD camera, Proscan, HS 101H
Control and automation	Fully motorized

As a result of the implemented upgrade programme today FLNP's optical platform on the basis of the "CARS" microscope is the only in its uniqueness for Raman and photoluminescence studies multimodal facility in Russia and CIS countries by its characteristics, parameters and functionality. <u>**It is also competitive at the world level.**</u>

3. Research programme

Expected main results by the theme completion:

- **Obtaining of highly contrast nonlinear chemical mapping of protein crystals with a signal to noise ratio not less than 30:1 in the P-CARS and SONICC options.**
- **First results aimed at achieving high sensitivity of organic molecules concentration detection level (10^{-8} – 10^{-10} M) using SERS as a newly developed modality at the multimodal optical platform.**
- **A complex study of the structural and spectral properties, including upconversion luminescence, of oxyfluoride glasses and glass-ceramics doped with various rare earth elements (REE).**
- **Completion of photo- and up-conversion luminescence of glass-ceramics based on nanoscale ZnO crystals and co-doped with Eu^{3+}/Yb^{3+} ions.**
- **Plasmonic photo- and upconversion luminescence enhancement (not less than one order of magnitude) – background for the further research activities in 2018-2020.**

3.1 Highly Sensitive P-CARS and SONICC Imaging of Protein Crystals

Water soluble and membrane proteins (MPs) are the functional units within cells. MPs serve vital functions such as ion and solute transport, energy and sensory transduction and represent roughly one-third of the proteins encoded in the human genome. However, although they are also extremely important drug targets (up to 60% of all existing drugs target MPs) they remain poorly characterized both functionally and structurally. Their crystallization and therefore structural investigation is still a great challenge. One of the most promising approaches is in meso MP crystallization, based on lipid containing crystallization matrixes, which made a key contribution to the crystallization of important proteins.

It's well known that serial crystallography at last generation X-ray synchrotron sources and free electron lasers enabled data collection with micrometer and even sub-micrometer size crystals which have resulted in amazing progress in structural biology. However, imaging of small crystals which although is highly demanded remains a challenge, especially in case of membrane protein crystals. In our present study we describe a new extremely sensitive method of the imaging of protein crystals which is based on polarization sensitive P-CARS technique.

It was already discussed in literature that CARS is sensitive for *in vivo* detection of lipid (cholesterol) crystals naturally occurring in the cells. However, until now CARS imaging of protein crystals has not been addressed. CARS may have important advantages and complementary to the existing protein crystals imaging techniques (for instance, SHG imaging) since it does not only

image crystals, but also may study the molecular composition of membrane protein crystals via the use of Raman scattering spectra lines specific for different molecules comprising a crystallization matrix and often the crystals. To have a reference for understanding the efficiency of P-CARS images we performed complementary SHG (SONICC) imaging of crystals studied via CARS. The CARS and SHG images are composed of 500x500 pixels taken by raster scanning the sample. Signal integration time was 3 μs/pixel.

As the first step to understand the CARS imaging potential we performed studies with *in meso* grown bacteriorhodopsin (bR) crystals. We investigated its structure and crystallization (including the studies of merohedral twinning) in great details and developed protocols of bR crystallization allowing us to regulate the size of the crystals, their quality and level of twinning. Our data obtained with lysozyme crystals support the idea of CARS general application to imaging of the crystals of biological macromolecules. In all experiments we used *in meso* grown BR crystals. The hexagonal crystal plates were with the sizes 1μm -100 μm in two dimensions and from about 0.5 μm to 20 μm thick. Very small crystals were used to estimate the limits of CARS sensitivity and spatial resolution.

Bacteriorhodopsin contains a chromophore retinal. The wavelength 568 nm corresponds to the maximum of bR absorption which is determined by the chromophore and the crystals have a characteristic purple color. The chromophore has a well studied Raman spectrum (**Fig. 3**).
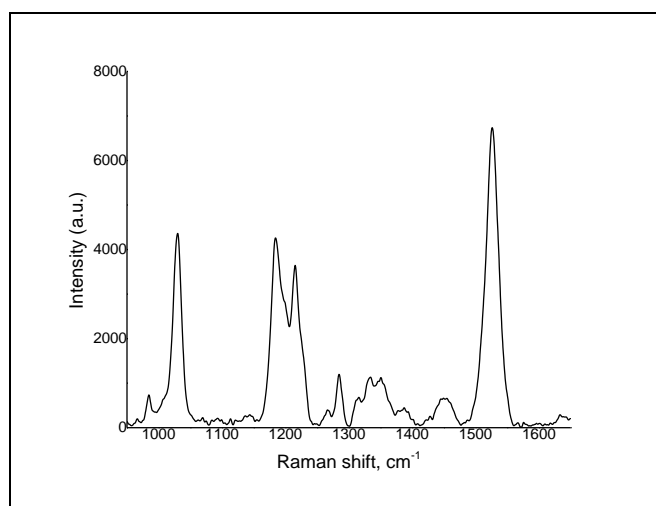

Fig.3. Raman spectrum of BR crystal

BR crystals were imaged directly in a crystallization well with selected C=C retinal chromophore Raman bands at 1529 cm^{-1} and 1570 cm^{-1}. First we compared P-CARS (polarized CARS) and F-CARS (forward CARS) images of bR crystals in the same crystallization probe. The hexagonal plane of some of the crystals is oriented along the image and some of them are perpendicular. With P-CARS (**Fig.4c,d and Fig.5**) the Raman bands display a higher signal to background ratio (of 30:1) in comparison with that of the F-CARS. Tuning the difference frequency ω_p-ω_S between the pump and the Stokes beams to 1570cm^{-1} resulted in an effective suppression of the nonresonant background in the P-CARS mode: the background signal almost disappears.
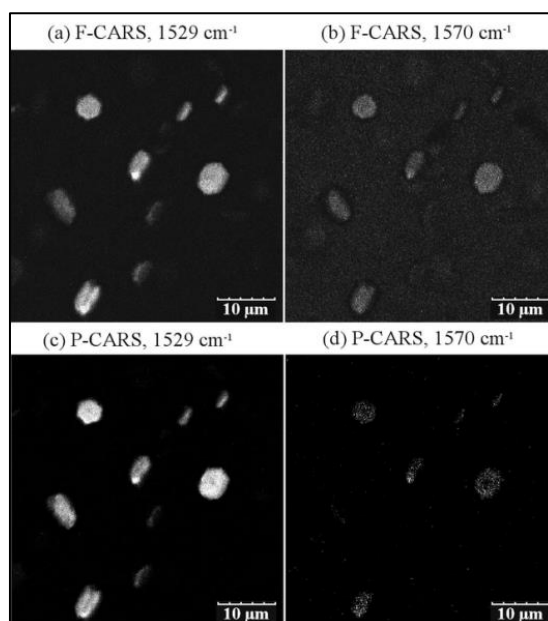
Fig.4. Comparison of F-CARS and P-CARS contrasts in resonant
and nonresonant conditions

To compare the sensitivity and resolution of P-CARS with those of the known methods (standard optical microscopy and SHG) we demonstrate in **Fig.5 (a-f)** the images of the crystals of different sizes. Though the difference between micrographs and transmission images is not very pronounced it is seen that the images under the monochromatic light (transmission) provide more structured images. Showing two types (micrograph and transmission) of images we aim to demonstrate that neither of them can compete with CARS for the quality of crystal imaging.
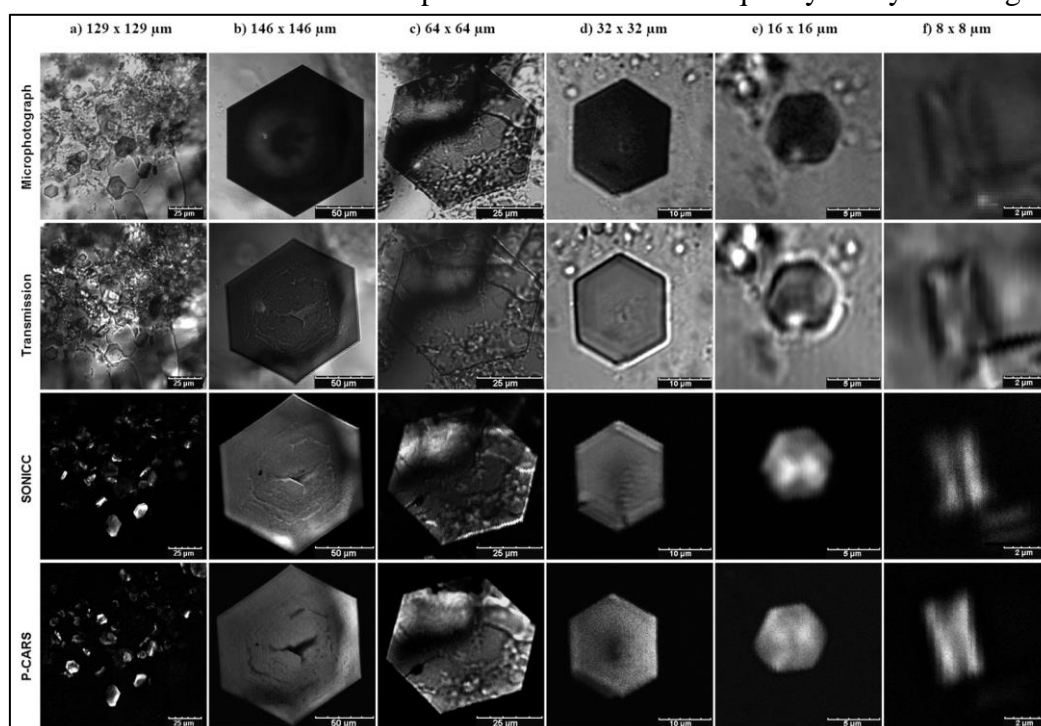
Fig.5
A gallery of micrograph, transmission, SHG (SONICC) and P-CARS images of bR crystals
acquired in various modes: a – panoramic picture of a crystallization probe, b, c – big crystals,
d – intermediate size crystals, e and f – very small crystals.

In case of the larger ones (30 μm and greater) all the techniques visualize the crystals well. However, only CARS and SHG are able to detect the defects of the crystals and CARS does this with a better contrast (**Fig.5b**). In the case of smaller crystals (less than 20 μm) the advantages of CARS and SHG are even more crucial (**Fig.5a**). Only they are able to identify important crystal features. **Thus, complementary application of CARS and SHG techniques provides a unique opportunity to study the growth of protein crystals on a large range of scales.**

Also, we observed with some of the crystals (**Fig.6**) that the shape and/or size of the same crystals imaged by CARS and SHG are different. We suggest that it happens in cases when some parts of the crystals are not well ordered. It is known that SHG signal is strong only when the crystal is well ordered. It is of interest because a complementary use of both methods can provide information about the level of order in crystal packing and help to select crystals preliminarily for X-ray crystallography. It can be very useful because quite often the crystals may have a perfect shape but do not diffract at all.
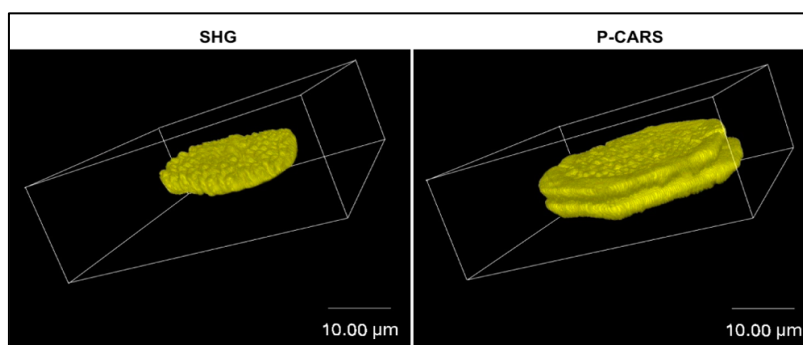

Fig.6. 3D SHG and 3D P-CARS images of a twinned bR crystal. Box size: 48x48x24μm

Amazing sensitivity of the P-CARS imaging is further demonstrated by detection and imaging of merohedrally twinned bR crystals (Fig.3). Merohedral twinning is one of the most common crystal-growth defects. Neither there is a fast approach to detection of twinned crystals nor is there an efficient method of the twinning-ratio determination. Twinned crystals cannot be optically distinguished. The only reliable method to detect twinning of the crystals is X-ray crystallography, which requires time-consuming X-ray data collection. In our work, we studied the potential of CARS for the detection of such crystals. **Fig.6** demonstrates that twinning of bR can be easily detected even in the case of small crystals with a micrometer size thickness, while SHG signal with 6ps excitation hardly discriminates the morphology of the twinned crystal if it partly consists of low ordered segments, as it is observed in our work. In contrast to X-ray crystallography, CARS makes the characterization of their morphology possible and demonstrates that the crystal consists of two nearly equal domains with the thickness about 2.5 μm.

Finally, we applied P-CARS for imaging of lysozyme crystals. Lysozyme is a water soluble protein also widely used in a number of investigations including the studies of mechanisms of water soluble protein crystal growth.

Thus, CARS, especially P-CARS, can be generally applied for fast, high resolution, high contrast and very informative imaging of protein crystals.

3.2 Detection of biomolecules by SERS spectroscopy

Surface-enhanced Raman scattering (SERS) combines spontaneous Raman spectroscopy with the local field enhancement capability of gold or silver nanostructures to amplify the signal. Discovered in 1974 SERS provides much greater sensitivity than conventional RS. The enhancement factor can be as high as 10^4 to 10^7. The enhancement mechanism originates in part from the large local electromagnetic fields caused by resonant surface plasmons that can be optically excited at certain wavelengths for noble metal nanoparticles (NPs) of different shapes, compact assemblies of NPs or noble metal nanostructures. The enhancement for Raman signals can be up to ~10^9-10^{11} if the analyte lies in so-called "hot spots", which are usually highly localized regions, typically at gaps between silver or gold nanostructures. Using ultrasensitive detectors, SERS allows for single molecule spectroscopy: since the local fields of metallic nanostructures can be highly confined, the lateral resolution can be two orders of magnitude better than the diffraction limit.

3.2.1 Detection of DNA molecules by SERS

Detection of DNA molecules today is widely used in many areas of human life such as medical diagnostics, gene therapy, forensic science, etc. For many years, the polymerase chain reaction and fluorescent spectroscopy have been the most popular methods used in practice to study DNA. Such methods are proven and reliable but often require expensive chemicals and take a long time to get results. Surface enhanced Raman scattering (SERS) spectroscopy is an alternative attractive way to study DNA with its remarkable ability of single molecule detection.

In our SERS experiments we used herring sperm DNA adsorbed on the silvered porous silicon (PS). Porous silicon has been fabricated by an electrochemical anodic etching of a highly doped n-type silicon wafer. It has been shown that the following silver immersion deposition on porous silicon lead to the formation of a layer of silver nano- and microparticles assembled in a quasi-ordered array (**Fig.7**). Reflectance spectroscopy has revealed that the silver layer demonstrates the surface plasmon resonance (SPR) band expanded to near-IR range (**Fig.7b**). Preliminary SERS measurements with rhodamine 6G have showed that the silvered porous silicon is characterized by a very good reproducibility of the SERS signal and one-year shelf life.
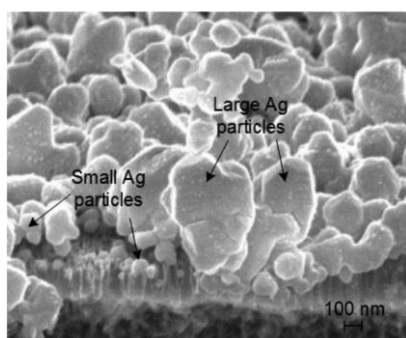

Fig.7 SEM top views of the PS samples after the immersion into 3mM AgNO$_3$ solution for 70 min.
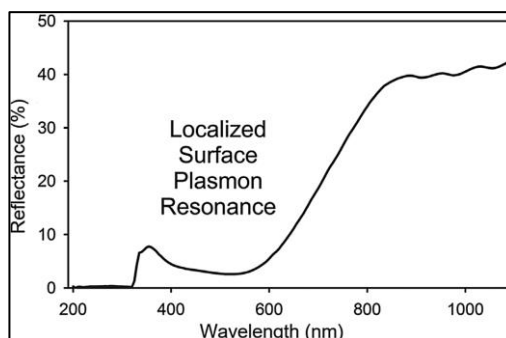
Fig.8 Reflectance spectrum of the PS samples after the immersion into 3mM AgNO3 solution for 70 min.

The Raman and SERS measurements of the herring sperm DNA were carried out under different laser wavelengths ranging from blue to near-IR regions (**Fig. 9**). It has been found that the

silvered porous silicon is SERS-active in relation to the herring sperm DNA under the laser excitation at 473, 633 and 785 nm.
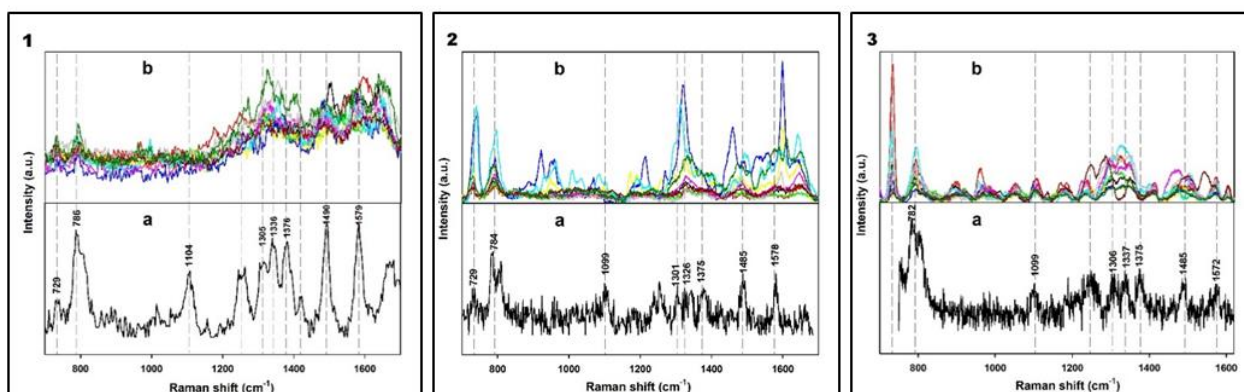

Fig.9. Raman (a) and SERS (b) spectra of the 10^{-8} M herring sperm DNA collected under the 473 (1), 633 (2) and 785 (3) nm laser wavelengths.

The peaks observed in the Raman spectra around 730 cm^{-1} (adenine), 787 cm^{-1} (thymine, cytosine), 1104 cm^{-1} (v(C–O), deoxyribose-phosphate), 1242 cm^{-1} (cytosine, adenine), 1381 cm^{-1} (thymine, guanine, adenine), 1490 cm^{-1} (guanine, adenine), and 1581 cm^{-1} (guanine, adenine) are the characteristic Raman bands of the herring sperm DNA molecules. SERS spectra were collected in 10 random points of the silvered PS. Remarkably, the silvered PS demonstrates SERS activity for all lasers employed in this study. The variations of the DNA SERS spectra mainly appear due to changes in molecules conformation after their deposition and drying on the silvered PS as well as an increase of randomness under laser irradiation. The intensity and the band position also depend on wavelength and power of the laser and accumulation time. For example, long UV radiation can destroy the DNA molecular group and bonds. Thus power of 473 nm laser was reduced about two orders of magnitude. Pronounced dominance of the adenine band is caused by its greater Raman cross section compared with that of guanine, cytosine, and thymine.
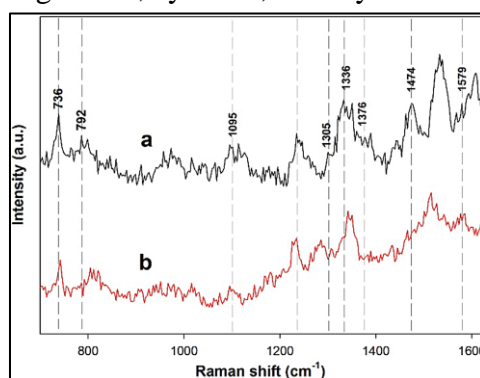

Fig.10 SERS spectra of the 10^{-8} M (a) and 10^{-10}M (b) herring sperm DNA, 473nm laser wavelength

Finally, the SERS mapping was used to detect the herring sperm DNA at an extremely low concentration of 10^{-10}M. In **Fig.10,** comparison of two SERS spectra of the DNA molecules at different concentrations is presented. The SERS spectra were recorded under the 473 nm excitation wavelength as both red and near-IR lasers showed no results for the lowest concentration.

The most promising result is in the detection of the DNA molecules at very low concentration (10^{-10} M) with the silvered PS. According to our knowledge, detection of such a small amount of DNA has not been reported elsewhere.

3.2.2 Detection limit of DPPC phospholipid by SERS

Detection limit is the smallest amount of analyte concentration in the sample that can be reliably distinguished from zero. Following this rule the lowest concentration of the analytes at which they are detectible was estimated when their less intensive related peak becomes unresolved at the noise level.

Phospholipids are ubiquitously presented in nature forming a bilayer of the cell membranes of all living tissues. They are responsible for the elastic properties of the membranes, stabilization of proteins within the membrane and transportation of lipids and fatty acids. Detection of their type, concentration and ratio in physiological liquids helps to recognize pulmonary, hepatic, sclerotic and many other diseases. Thus sensitivity of the detection technique plays an important role in early diagnostics. Thin-layer chromatography and single molecule fluorescence spectroscopy have been already demonstrated to meet this requirement. However, their practical application is limited by a complicated sample preparation, necessity to use specific markers and difficulties in interpretation of the results obtained.

Reference Raman and SERS spectra corresponding to DPPC molecules are presented in **Fig. 11**. The Raman spectrum was recorded for the solution containing 10^{-2} M of DPPC deposited onto SERS-inactive substrate. The observed peaks at 718 cm^{-1} (choline C–N stretch), 769 cm^{-1} (O–P–O sym. stretch), 869 cm^{-1} (trans C–C stretch), 957 cm^{-1} (P–O sym. stretch), 1065 cm^{-1} (acyl chain trans C–C stretch), 1093 cm^{-1} (acyl chain gauche C–C stretch), 1127 cm^{-1} (acyl chain trans C–C stretch), 1297 cm^{-1} (acyl chain CH2 twist), and 1449 cm^{-1} (CH$_2$ bend) corresponds to this compound.
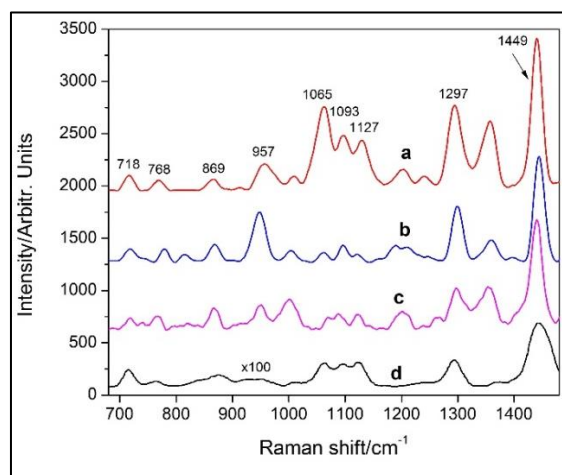

Fig.11 (a, b, c) SERS and (d) Raman spectra of (a) 10^{-6} M, (b) 10^{-9} M, (c) 10^{-12} M and (d) 10^{-2} M DPPC collected at the at the 633 nm wavelength.

Three upper curves in Figure 11 represent SERS signals from the dried solutions containing DPPC in concentrations between 10^{-6} and 10^{-12} M. The laser wavelength was 633 nm. Positions of the SERS peaks are evident to correlate with the reference Raman peaks while some small deviations are observed. **The lowest concentration at which of DPPC was detected is estimated to be 10^{-12} M.**

3.3 Raman spectroscopy:comparing the "fingerprints" of C6 glioma and stem cells

Number of studies demonstrated analogies between tumor cells and stem cells – self-renewal mechanisms, organogenic capacity, cases when normal stem cells mutate acquiring tumor-initiating properties and driving tumor formation. Intriguing similarity between the normal stem-cells from neurogenic regions of mammalian brain and tumor-initiating cells of glioma led to the suggestion that tumor stem-like cells may contribute to gliomagenesis.

In the present study we compared Raman scattering spectra of undifferentiated glial tumor (C6 glioma cell) and mesenchymal stem cells (MSC). Raman spectroscopy is a sensitive analytical technique capable of providing highly detailed biochemical information on the biological samples. In particular, it can be used to distinguish between normal and malignant tissues. Our goal was to see whether the difference exist at the stage when cancerous and wholesome cells are undifferentiated.
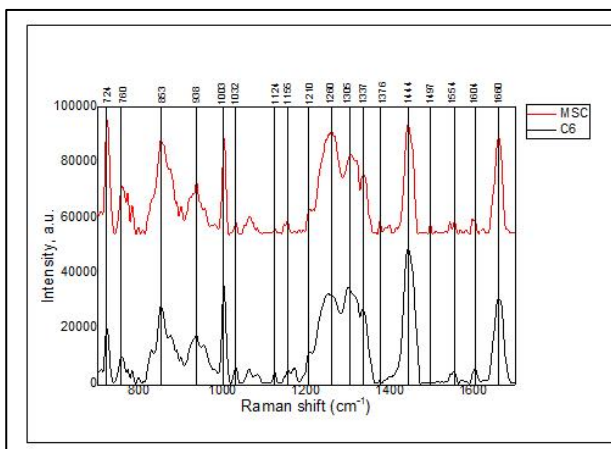

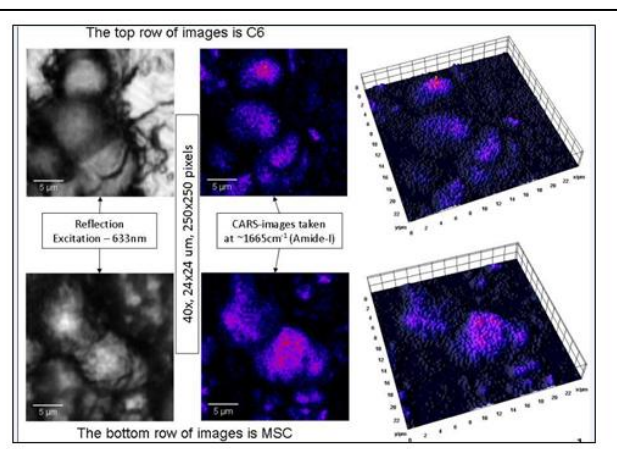**Fig.19.** The comparison of Raman spectra of rat's MSC and C6 glioma cells.

Fig.20 Micrographs and CARS images of rat's MSC and C6 glioma cells

Raman spectroscopy **(Fig.19)** and CARS microscopy **(Fig.20)** revealed a striking similarity of scattering spectra from rat's MSC and C6 glioma cells. This is in contrast to the study comparing the spectra from the formed tumor versus normal differentiated tissue. In our opinion, there is one important detail in obtained data: we compared undifferentiated MSC and C6 glioma cells. Therefore, namely the fact of insufficiency (or absence) of differentiation is the basis of revealing the identity mechanism of C6 glioma and MSC Raman scattering spectra. So, accumulated data from Raman spectra and CARS microscopy speak for being them potential instrument for differential diagnostics and especially for intraoperative demarcation of tumor and healthy tissue.

Our results indicate possible relations between the MSCs and C6 glioma cells, which is in accordance with the studies reporting expression of common antigens in stem cells and various types of tumor.

Thus, we demonstrate that at some stages of development and metabolic activity malignant cells and normal stem cells can have nearly identical "fingerprints" (Fig.19,20 present similar in every detail Raman spectra of mesenchymal stem cells and C6 glioma cells: amides, phenylalanine, lipids, peptides). This phenomenon helps to understand the difficulty encountered by immune defense system in tumor-bearing organism, showing one of the ways for tumor cells to escape from protective activity of immune cells. Our results also show a potential pitfalls in the cancer diagnostics.

3.4 Upconversion luminescence in glass-ceramics containing Er:PbF$_2$ nanocrystals

Development of high-techs claims production of stable, energy-conserving and eco-friendly equipment. One of such techniques in optics is based on the upconversion effect. The basic ideas on upconversion were generated more than 50 years ago in papers by Bloembergen and Auzel. Later, for several decades this process, which is actually an anti-Stokes type of radiation, was widely studied by many authors and had several important applications among which are shortwave lasers, various opto-electronic devices, biophosphors, etc. To date the interest to the phenomenon of upconversion has received a new impulse due to the synthesis of modern matrix elements that contain various nanocomposites.

Upconversion is most effective in doping of optically inert matrices with lanthanide ions. Fluorides, bromides, chlorides, iodides and other materials are most often used as glass matrices with low-phonon energy environment. Such environment prevents non-radiative losses of energy in the excited states of lanthanide dopants. Oxyfluoride glasses and based on them nanoceramics, that combine benefits of low-phonon energy of fluorides, chemical durability and mechanical stability of oxides, and high optical quality of silicate glasses are of special interest. We used the opportunity to register the medium response to the IR laser excitation in the anti-Stokes region of the spectrum for up-conversion luminescence studies.

Up-conversion is a process where absorption of several pump photons is followed by emission of one high-energy photon (with a shorter wavelength). In this way, near-IR-to-visible conversion is possible typically with the rare-earth ions. Trivalent erbium, Er^{3+}, is suitable for such conversion due to the special structure of energy levels allowing for population of higher-lying excited states via the excited-state absorption, cross-relaxation, and energy-transfer mechanisms. Intense green and red (centered at ~540 and 650 nm) up-conversion luminescence (UCL) from Er^{3+} ions was studied previously for a large variety of glasses, glass-ceramics, single-crystals and nano-powders following the pioneering work of F. Auzel et al. The potential applications of such Er-doped phosphors are in the field of solid-state lightning, biological labeling, or enhancing solar-cell efficiency; Er up-conversion visible lasers were also reported.

An important point for the efficient up-conversion is the rate of non-radiative relaxation from the involved excited-states. This rate depends on the maximum phonon frequency of the host; so fluoride materials provide better up-conversion properties due to lower phonon frequencies, ~500–600 cm^{-1} (as compared with their oxide counterparts). Oxyfluoride glass-ceramics (GC) is the compromise material with fluoride nanocrystals nearly uniformly distributed in the residual predominantly oxide glassy phase. It allows for a combination of good spectroscopic properties of fluorides with chemical stability and good thermal and mechanical properties of oxide compounds. GC can also be synthesized by a standard melt-quenching technique with subsequent heat treatment.

In this study transparent oxyfluoride germanosilicate glass-ceramics containing Er:PbF$_2$ nanocrystals is synthesized on the basis of SiO$_2$–GeO$_2$–PbO–PbF$_2$ initial glass doped with Er$_2$O$_3$. For the preparation of GC, the as-cast glass was heat-treated at 350ºC (slightly below the T_g temperature) for 10–30 h. The glass-ceramics was transparent with a slight rose color. Its XRD pattern is shown in **Fig.12a,** together with the peaks corresponding to a bulk β-PbF2 crystal. In

addition to a characteristic halo of the residual glassy phase, sharp diffraction peaks are observed corresponding to that of PbF_2 compound. The mean size of the nanocrystallites determined with the Scherrer equation is 8.5 ± 0.5 nm.
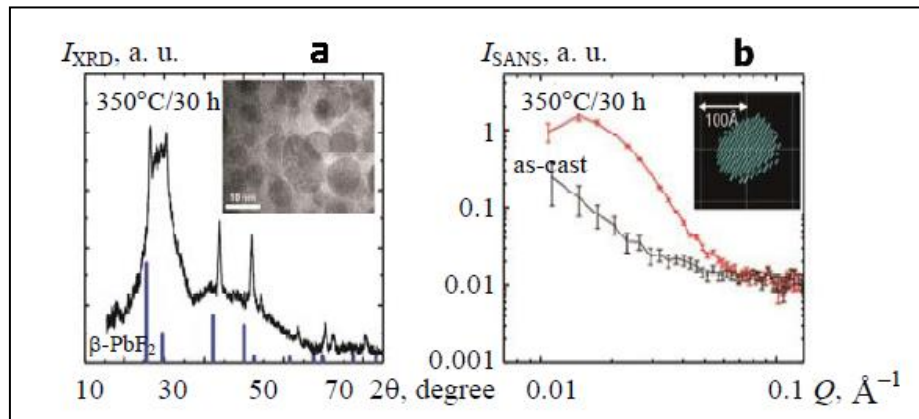

Fig.12

a) XRD pattern of GC heat treated at 350°C/30 h; vertical lines correspond to the peaks of the bulk β-PbF_2 crystal; the inset represents an HR-TEM image;

b) intensity of the SANS vs the modulus of the scattering vector, Q, for the precursor glass and GC; the inset represents a ATSAS modeled shape of the nanocrystal.

For a structural characterization of the GC, we also used small-angle neutron scattering (SANS), with an IBR-2 reactor as the source of the pulsed neutron flux and an YuMO spectrometer. The scattering intensity vs modulus of the scattering vector Q for both the as-cast glass and GC treated for 30 h is plotted in **Fig.12b**. The heat treatment induces a substantial change of the glass structure, which is clear from the scattering curves with a characteristic peak. To model the shape of the nanocrystals (inset in Fig.12b), we used the ATSAS software. The mean size of PbF_2 nanocrystals is around ~10 nm, which is consistent with XRD and HR-TEM data.

The morphology of the GC is recorded using SEM. The corresponding micrograph is shown in **Fig.13.**
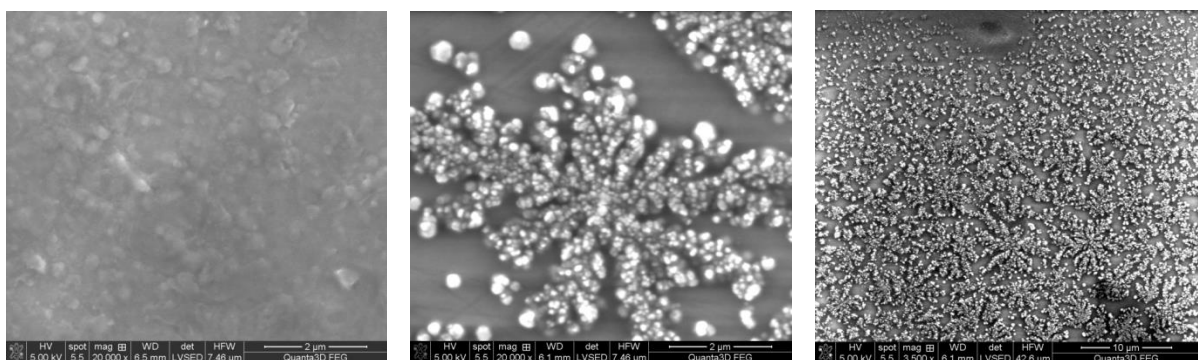

Fig.13 SEM images of precursor (left) and glass-ceramics (middle and right).

Obviously, the precursor glass is amorphous. The shape of the Er^{3+}:PbF_2 nanocrystals in glass-ceramics appears to be of dendritic and not spherical shape. Dendritic nanoparticles seem clearly constituted of several crystallites.

Absorption and upconversion luminescence (UCL) spectra.

Absorption spectra of Er^{3+} ions were measured at the spectrophotometer Varian Cary 5000. **Fig.14** illustrates the absorption spectra measured over the ranges of: (a) 500-570 nm, (b) 630-700 nm and (c) 780-820 nm.
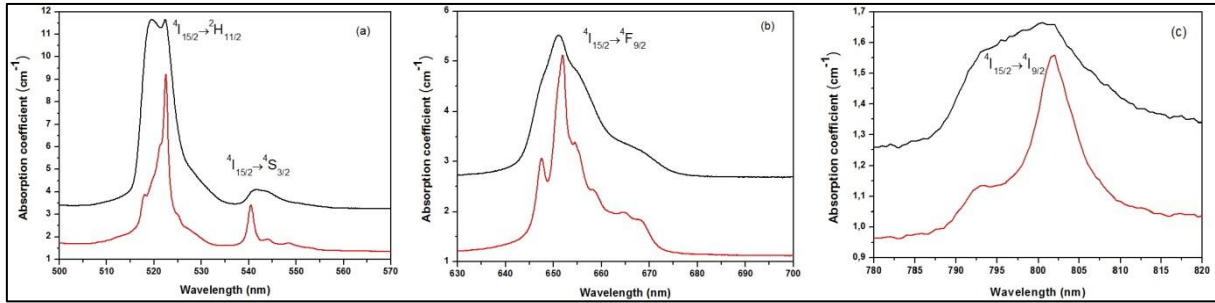

Fig.14 Absorption spectra measured over the ranges of: (a) 500-570 nm, (b) 630-700 nm and (c) 780-820 nm. The black curve – precursor glass, the red curve – glass-ceramics.

Three absorption bands were recorded in the visible part of the spectrum corresponding to the transitions: $^4I_{15/2} \rightarrow {}^2H_{11/2}$ (520 nm), $^4I_{15/2} \rightarrow {}^4S_{3/2}$ (540 nm) and $^4I_{15/2} \rightarrow 4F_{9/2}$ (650 nm). One more spectral band was recorded in the near IR range with the maximum centered around 800 nm that corresponds to the transition $^4I_{15/2} \rightarrow {}^4I_{9/2}$.

The UCL in the glass and GC was excited at ~980 nm wavelength. The UCL spectra of the Er-doped glass and glass-ceramics are shown in **Fig.15a,b.** Both of them are normalized to unity for comparison. For the as-cast glass, the green emission dominates. The two closely located bands centered at 522 and 544 nm are related to the transitions from the $^2H_{11/2}$ and $^4S_{3/2}$ excited states to the $^4I_{15/2}$ ground state. The weak red band contains two components at 653/667 nm; it is related to the transition $^4F_{9/2} \rightarrow {}^4I1_{5/2}$. The deep red bands at ~800 and 845 nm are related to the transitions $^4I_{9/2} \rightarrow {}^4I_{15/2}$ and $^4S_{3/2} \rightarrow {}^4I_{13/2}$, respectively.
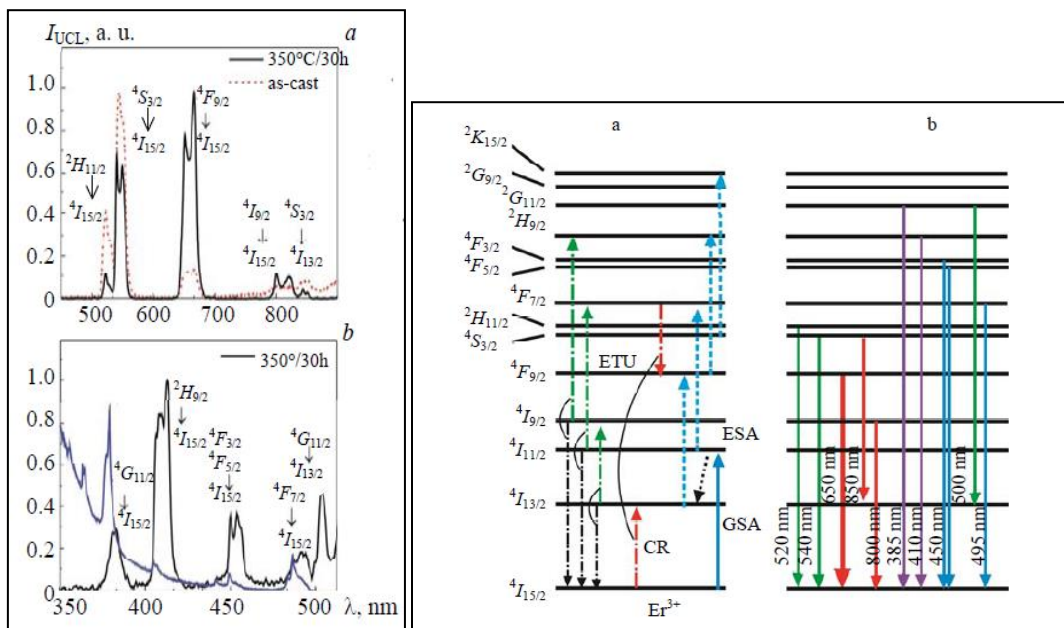

Fig.15 Left: UCL spectra for the GC treated at 350 °C/30 h and the as-cast glass (a,b); **Right: t**he scheme of the energy levels of Er^{3+} ions in the studied GC

No emission at the wavelength shorter than 500 nm is detected, at least at an excitation power density of ~104 W/cm^2. This determines the green color of the emission from the as-cast glass. The calculated Commission Internationale de l'éclairage (CIE 1931) color coordinates are $x = 0.268$ and $y = 0.608$; the dominant wavelength is 545 nm with 0.95 color purity.

The scheme of energy levels of Er3+ ions showing the potential channels of their excitation and observed UCL lines is shown in Fig.15 (right). Ground-state absorption (GSA) corresponds to $^4I_{15/2} \rightarrow ^4I1_{1/2}$ transition. Several excited-state absorption (ESA) channels exist for Er^{3+} ions.
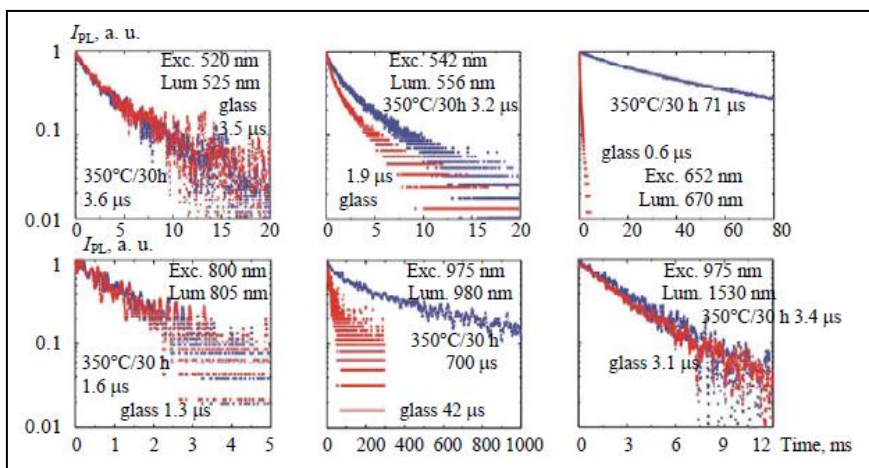

Fig.16 Decay curves for the visible and IR luminescence of Er-doped glass and GC

The UCL intensity depends on the lifetime of the excited state, from which the radiative transition occurs (**Fig.16**). For the green UCL, these are the states $^2H_{11/2}$ and $^4S_{3/2}$; for the red UCL, this is $^4F_{9/2}$. Also, I_{UCL} depends on the lifetime of the intermediate state, from which the excitation steps (like ESA) occurs. If this lifetime is long enough, the probability of further excitation increases (with respect to luminescence to the ground state or non-radiative relaxation). However, the shortening of the lifetime of the intermediate state can also work as a switch of different emission channels. This occurs for the $^4I_{11/2}$ state of Er^{3+} ions. If its lifetime is long, the $^4I_{11/2} \rightarrow ^4F_{7/2}$ ESA process dominates, resulting in the strong green UCL. If it is short, fast non-radiative decay leads to the $^4I^{11/2} \rightarrow ^4I_{13/2}$ relaxation and alternative $^4I_{13/2} \rightarrow ^4F_{9/2}$ ESA channel, leading to the strong red UCL. The change of the environment of the Er^{3+} ions from the oxyfluoride (glassy) to pure fluoride (crystalline, PbF$_2$) can disturb all the above-mentioned lifetimes.

After the heat treatment of the as-cast glass, the lifetime of the $^4S_{3/2}$ state is increased only to 3.2 μs, which means a slight enhancement of the green emission. For the less intense transition from the $^2H_{11/2}$ state, the lifetime is nearly the same (3.6 μs). In contrast, the lifetime of the $^4F_{9/2}$ state is increased more than 100 times, to 71 μs. This is the key point to understanding the redistribution of intensity from green to red bands in the UCL spectrum of the glass-ceramics. The lifetime for the intermediate state, $^4I_{11/2}$, is nearly 16 times longer (as compared with the as-cast glass). This prevents complete suppression of the green UCL for the glass-ceramics.

Novel transparent oxyfluoride germanosilicate glass-ceramics containing Er:PbF$_2$ nanocrystals are synthesized on the basis of the SiO$_2$–GeO$_2$–PbO–PbF$_2$ initial glass doped with Er$_2$O$_3$ by a secondary heat treatment. GC is characterized by an intense yellow-green emission. The redistribution of intensity between the green and red emissions with the heat treatment is explained from the point of view of the lifetime measurements. The mechanisms of the UCL for 11 lines in the UV, visible, and near-IR are explained.

3.5 Photoluminescence of transparent glass-ceramics based on ZnO nanocrystals and co-doped with Eu³⁺, Yb³⁺ ions

ZnO is an intensively studied wide band gap semiconductor (E_g =3.37 eV) with various applications especially, in optoelectronics. ZnO has been reported as a promising host for rare earth (RE) ions. In recent years, there has been increasing interest in the development of RE ions doped ZnO quantum dots. RE ions doped glass-ceramics (GC) containing ZnO nanosized crystals are alternative materials to RE ions doped ZnO quantum dots as oppositely to quantum dots, ZnO nanocrystals are homogeneously distributed within the glass matrix without agglomeration. The materials are produced by a convenient melt-quenching technique, the properties are highly reproducible and are not deteriorated during storage. However, after the pioneer paper of L. Pinckney, there have been only few papers on spectral properties of GC containing volume crystallized ZnO nanocrystals including those doped with ions of transition and rare-earth (RE) elements, despite these materials show promise for the development of laser technology and optoelectronics.

In our studies a glass with the composition (mol%) $14K_2O–32ZnO–14Al2O3–40SiO_2$ was co-doped with 1 mol% Eu_2O_3 and 1 or 1.5 mol% Yb_2O_3 added above 100% of the base components. Transparent zincite (ZnO) glasseceramics were obtained by secondary heat treatments at 680–860 ^{o}C. X-ray diffraction (XRD) patterns of the powdered initial glasses and GC were measured using a Shimadzu XRD-6000 diffractometer, Cu K_a radiation with a Ni filter (**Fig.17**).
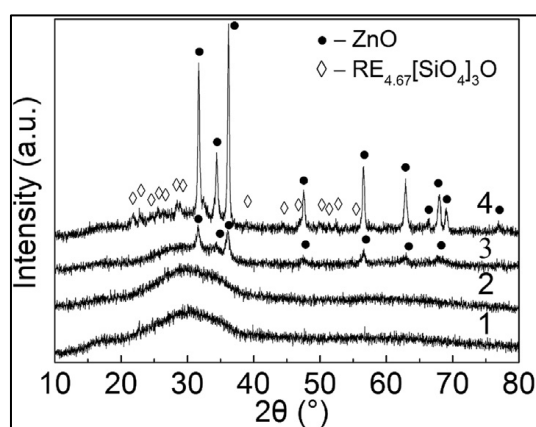

Fig.17. XRD patterns of the initial glass co-doped with 1 mol% Eu_2O_3 and 1.5 mol% Yb_2O_3 (1), initial glass co-doped with 1 mol% Eu_2O_3 and 1 mol% Yb_2O_3 (2), and GC doped with 1 mol% Eu_2O_3 and 1 mol% Yb_2O_3 and heat-treated at 680°C for 12 h (3), and at 860°C for 2 h (4).

It is seen that both initial glasses are X-ray amorphous. Zinc oxide nanocrystals with a size of ~14 nm appeared after the heat treatment of the initial glass co-doped with 1 mol% Eu_2O_3 and 1 mol% Yb_2O_3 at 680°C for 12 h. Thus obtained GC sample is transparent. The XRD pattern of the GC prepared by the heat treatment at 860°C for 2 h demonstrates crystallization of two phases, i.e., ZnO crystals with a size of ~35 nm and traces of oxyapatite crystals. The ZnO crystallinity fraction increases about 4 times with increasing heat-treatment temperature. The sample is translucent.

Photoluminescence (PL) and photoluminescence excitation (PLE) spectra were recorded in the spectral range from 0.25 to 0.90 mm using an MDR-23U single-beam grating monochromator with the focal length of ~0.6 m and a diffraction grating with 1200 grooves per mm (reciprocal

linear dispersion 13 Å/mm). All spectra were measured using a DKSELe1000 xenon lamp with a power of 1000W as a light source.
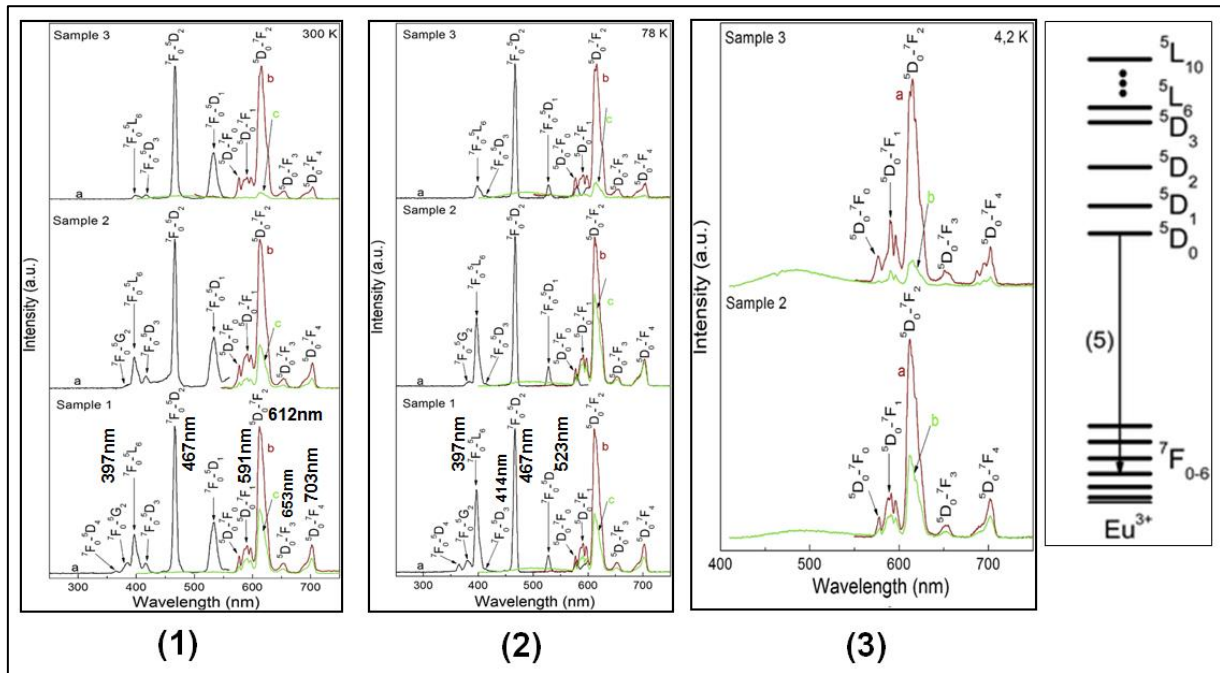

Fig.18 Normalized PLE (a) and PL spectra for glass (Samp.1) and GC (Samp. 2,3) recorded at the excitations: 467 nm (b) and 397 nm (c) at room temp.(1); at 78K (2), and at 4.2K (3).

Fig.18 shows PLE spectra and PL spectra taken at room temperature (~300 K) for the glass (the sample 1) and the GCs (samples 2,3). The PLE spectra of all samples were recorded in the spectral region from 250 to 550nm with a spectral resolution of ~2 nm with their detection at ~612 nm corresponding to the maximum of the luminescence band due to the $^5D_0$-$^7F_2$ electronic transition.

Our experiments demonstrated that the intensity and the spectral shape of the luminescence and absorption bands in the PLE spectra depend on the temperature and duration of heat treatment, as heat-treatments influence both the nature of the precipitating crystalline phases and the crystallinity fraction of the samples. This accordingly influences the nearest surrounding of the luminescent Eu3+ ions. Nor can we rule out the RE ions entering into the ZnO nanocrystals, which may result not only in redistribution of radiative recombination channels but also in creation of new radiationless recombination centers leading to degradation of luminescence signals. According to the PL measurements at room temperature, we revealed that with increasing the heat treatment temperature and, accordingly, the fraction and the size of ZnO nanocrystals, the integral intensity of the luminescence bands of the Eu3ю ions decreases by approximately 10% for the sample 2 and by 13% for the sample 3.

The study of the luminescence properties of the ZnO nanocrystal-containing GC doped with Eu^{3+} ions revealed intense PL from intracenter f-f optical transitions of Eu^{3+} ions. High intensity intrinsic exciton emission from ZnO nanocrystals was observed for the first time in Eu^{3+}-doped GC. It is assumed that some of the Eu^{3+} ions can be captured by ZnO anocrystals during crystallization. The mentioned results show that RE doped glass and GC based on ZnO nanocrystals are promising materials for optical applications.

4. Student programme

1) 2015 – 2016: 3 students – defense of bachelor's degree

2) 2016 – 2017: 3 students, current preparation of master's theses

3) 2016: 8th JINR UC Summer School, Practical training of students and postgraduates from Egypt

4) 2 students, Summer Student Program and practical training in 2016 (JINR UC)
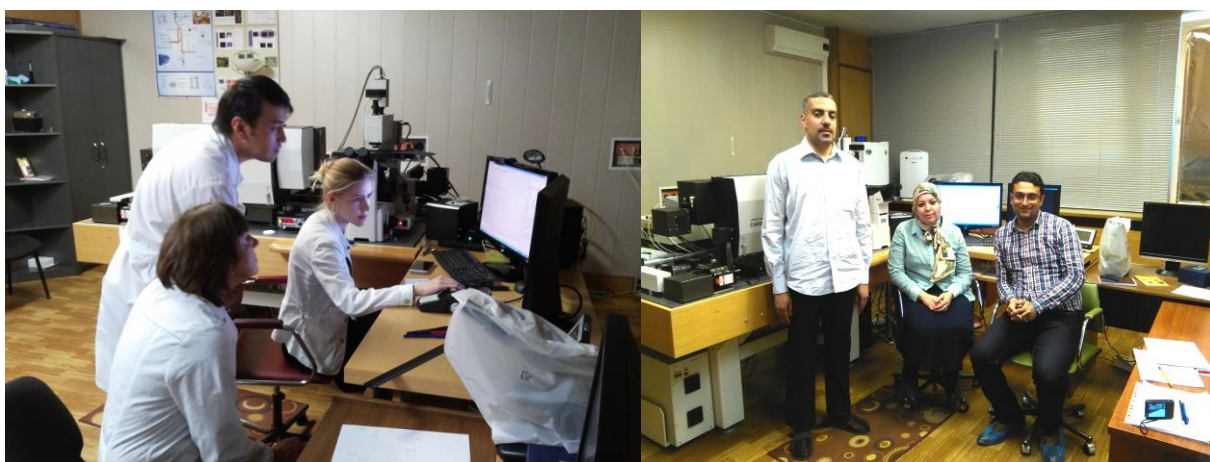
International cooperation: Armenia, Belarus, Germany, Uzbekistan, Latvia, Moldova, Poland, Russia, Romania, Ukraine, France.

Total number of publications – 17

Number of conferences - 23

5. Main publications and patent

1. Arzumanyan G.M., Doroshkevich N.V., Mamatkulov K.Z., Gordeliy V.I., et al., "Highly Sensitive Coherent anti-Stokes Raman Scattering Imaging of Protein Crystals", JACS, 2016, Volume 138(41), pp. 13457-13460

2. Arzumanyan G.M., Kuznetsov E.A., Zhilin A.A., et al., "Photoluminescence of transparent glass-ceramics based on ZnO nanocrystals and co-doped with Eu3+, Yb3+ ions", J. Optical Materials, 62, 2016, 666-672

3. Girel K., Yantcevich E., Arzumanyan G, et al., "Detection of DNA molecules by SERS spectroscopy with silvered porous silicon as an active substrate", Phys. Status Solidi A, 1–5 (2016) / DOI 10.1002/pssa.201600432

4. Othman H.A., Arzumanyan G.M., Moncke D., "The influence of different alkaline earth oxides on the structural and optical properties of undoped, Ce-doped, Sm-doped, and Sm/Ce co-doped lithium alumino-phosphate glasses", J. Optical Materials, 62, 2016, 689-696

5. Arzumanyan G.M., Mamatkulov K.Z., Fabelinsky V.I., et al., "Surface Enhanced CARS from Gold Nanoparticle-Immobilized Molecules at Cerium Dioxide/Aluminium Film", Technical Digest (Nanophotonics and Plasmonics) of Int. Conf. ICONO/LAT 2016, p. 88-89, Minsk, Belarus, September 26–30, 2016.

6. Kaniukov E.Yu., Belonogov E.K., Arzumanyan G.M., et al., "Features of forming of copper deposit in pores of silicon oxides", Proceedings of the NAS of Belarus, Physico-Technical series 2016, # 3, pp 11-15

7. O.Yu. Poimanova, A.O. Medvid, I.S. Kolomets, G.M. Arzumanyan, "Synthesis of barium isopolytungstates from aqueous dimethylformamide solutions", Nauka Kubani, 2016, #4, 4-11

8. Arzumanyan G.M., Kulchitsky V.A., Dosina M.O., Mamatkulov K.Z., et al., JSCRT, Vol. 1(1), Dec. 2016

9. P.A. Loiko, G.E. Rachkovskaya, G.M. Arzumanyan, et al., "Mechanisms of upconversion luminescence in glass-ceramics containing Er:PbF$_2$ nanocrystals", J. Appl. Spectr., 2017, 84(1)

10. Arzumanyan G.M., Mamatkulov K.Z., Fabelinsky V.I., et al., "Surface Enhanced micro-CARS from Gold Nanoparticle-Immobilized Organic Molecules", Int. conf. ECONOS, 2-5 April, 2017, Jena, Germany, Technical Digest, pp.73-74

11. V. Polovinkin, D. Willbold, G. Arzumanyan, J.-L. Popot, V. Gordeliy, et al., "Nanoparticle Surface-Enhanced Raman Scattering of Bacteriorhodopsin Stabilized by Amphipol A8-35", J. Membrane Biol (2014), 247, 971–980

12. Patent of the Russian Federation, "Luminescent glass-ceramics", # 2579056, 02.03.2016